University of BRISTOL

Link to publication record in Explore Bristol Research
PDF-document

University of Bristol - Explore Bristol Research
General rights

The effects of residual stress on elastic-plastic fracture propagation and stability

H.E. Coules [a,*], G.C.M. Horne [a], K. Abburi Venkata [a], T. Pirling [b]

[a] Department of Mechanical Engineering, University of Bristol, Bristol, UK
[b] Institut Laue Langevin, Grenoble, France

HIGHLIGHTS

- Residual stresses affect the resistance of materials to crack initiation, but also their resistance to crack growth.
- Consequently, residual stress can strongly affect fracture stability even in non-brittle conditions.
- Lei's modified J-integral predicts elastic-plastic crack advance well in the presence of residual stresses.
- Plastic relaxation of residual stress can occur during non-brittle fracture; this affects subsequent fracture resistance.

GRAPHICAL ABSTRACT
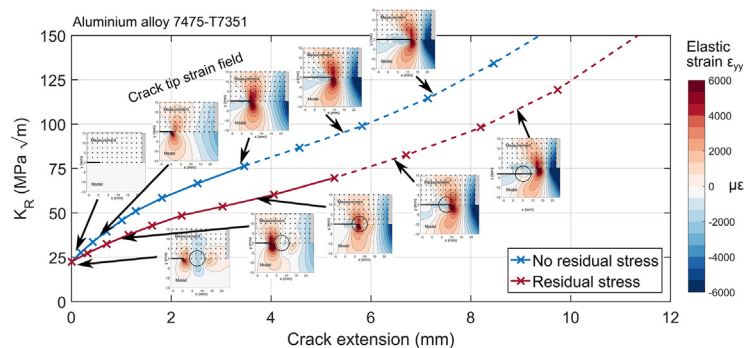
ABSTRACT

Residual stresses in materials affect their resistance to the initiation of fracture and to subsequent crack growth. Using full-field strain measurements and finite element analysis we demonstrate that the effect of residual stress on a material's crack growth resistance curve can be understood using elastic-plastic fracture mechanics. It is shown that Lei's modified J-integral formulation (J_{mod}) is a good predictor of the load vs crack extension behaviour of an elastic-plastic material containing residual stresses.

© 2018 The Authors. Published by Elsevier Ltd. This is an open access article under the CC BY license (http://creativecommons.org/licenses/by/4.0/).

1. Introduction

Residual stresses in structural materials can affect the initiation of fracture at pre-existing cracks by modifying the intensity of the crack tip stress field [1]. When stresses due to externally-applied loading occur together with residual stresses, their effects on the crack tip stress field superimpose. Therefore, depending on whether they favour crack opening or crack closure, residual stresses can either promote or inhibit the initiation of fracture. In a linearly-elastic material, the effects of residual and applied stresses on the Mode I stress intensity factor K_I superimpose perfectly. K_I is then simply the sum the stress intensities imposed individually by residual stress and applied loads [2]:

$$K_I = K_I^A + K_I^R \tag{1}$$

where K_I^R and K_I^A are Mode I stress intensity factors resulting from residual and applied components of the stress field respectively. For a brittle

* Corresponding author.
E-mail address: harry.coules@bristol.ac.uk (H.E. Coules).

material that exhibits almost perfect linear elasticity up to the point of fracture initiation, this leads to the following fracture initiation criterion:

$$K_{Ic} \leq K_I^A(a_0) + K_I^R(a_0) \tag{2}$$

where K_{Ic} is the material's Mode I initiation fracture toughness and a_0 is the initial crack length.

In materials that exhibit non-linear load-elongation behaviour prior to fracture initiation the contributions of residual and applied loading to the crack driving force combine non-linearly [2], and consequently Eq. (2) is not an accurate criterion for fracture initiation. The presence of residual stress affects the crack tip stress field and distribution of plastic strain that develops around the crack tip as it is loaded [3]. Consequently, the effect of residual stress on the strain energy release rate is not simply additive with the effect of applied loading [2,4]. In a finite element model of an elastic-plastic object, it is possible to impose a residual stress field explicitly and then calculate the Rice J contour integral that occurs at a crack tip in the object as it is loaded [5]. The J-integral does not rigorously characterise the crack tip stress field in an inelastic material, nor in the presence of initial strains. However, a modified form of the J-integral developed by Lei has been used as a predictor of elastic-plastic fracture initiation in real inelastic materials subject to residual stress [6].

The relative contributions of applied loading and residual stress to the strain energy release rate at cracks in nonlinear materials are significant in the assessment of safety-critical structures. The R6 Rev. 4 [7] and BS 7910 [8] structural integrity assessment procedures both use a plasticity correction factor V to account for non-linearity in the superposition of stress intensity factors resulting from applied and residual stress loadings [9]:

$$K_{Ic} \leq K_I^A(a_0) + V K_I^R(a_0) \tag{3}$$

This expression conveniently enables the prediction of elastic-plastic fracture initiation in the presence of a combination of applied and residual stress. The factor V may be calculated using finite element analysis or taken from pre-calculated tables listing values of V that are intended to be conservative for most geometries [7].

The effective fracture toughness of most materials changes significantly as a crack extends. In relatively ductile metals, the fracture resistance generally increases during the initial stage of crack propagation [10]. This characteristic is known as a rising resistance curve (R-curve). Factors that contribute to a rising R-curve include initial blunting of the crack tip in ductile materials, progressive development of the plastic zone ahead of the crack tip as the material strain-hardens, and progressive loss of constraint at any intersections between the crack front and free surfaces [11,12]. Just as they affect initiation fracture toughness, residual stresses also affect the R-curve behaviour of materials [13]. However, the residual (i.e. self-equilibrating) component of the stress field at a loaded and propagating crack in a ductile material can be changed both by crack extension and by plastic deformation at the crack tip [1]. Consequently the effect of residual stress on the R-curve in non-brittle materials is complex and it has not been extensively studied. In summary, the following factors determine the R-curve of a residually-stressed material:

1. The inherent R-curve of the material in a homogeneous and residual-stress-free state.
2. The initial residual stress field that exists in the material prior to fracture initiation.
3. Any changes in residual stress resulting from crack extension during fracture.
4. Any changes in residual stress resulting from plasticity during fracture.

5. Any initial inhomogeneity in the material's local inherent fracture toughness that the crack tip encounters during fracture.

Measurement techniques that allow full-field mapping of the strain field surrounding a crack tip include digital image correlation (DIC) [14], Electronic Speckle Pattern Interferometry (ESPI) [15] and photoelasticity [16,17]. Additionally, synchrotron X-Ray Diffraction (XRD) and Neutron Diffraction (ND) can be used to measure elastic strain point-wise at the interior of polycrystalline materials. Using a large number of measurements, these techniques can build up a map of the crack tip region [18–20]. Synchrotron XRD mapping of the crack tip strain field in this manner has previously been used to study the effect fatigue crack growth [19,21].

In this study, the R-curve behaviour of residually-stressed 7000-series aluminium alloy has been investigated in detail. Changes in residual stress during crack extension were observed using ND and DIC. Using Finite Element Analysis (FEA), these changes were related to the strain energy release rate and to plastic deformation at the crack tip.

2. Experiments

2.1. Specimen preparation and fracture tests

The experiments used Compact (Tension) specimens of aluminium alloy 7475-T7351. This is a precipitation-hardened 'high-strength' wrought alloy which exhibits a rising crack growth resistance curve. All of the specimens were in the L-T orientation relative to the parent plate [22]. The sequence of operations used in specimen preparation is shown in Fig. 1a. First, 18 mm-thick rectangular specimen 'blanks' were machined. Half of these were indented using a load of 75 kN applied through a pair of cylindrical indentation tools with a diameter of 8 mm at the location shown in Fig. 1b. To ensure a consistent specimen size, the specimens were reduced to a thickness of 15 mm by removing an equal thickness of material from opposite faces. The crack was introduced using wire Electrical Discharge Machining (EDM) and fatigue pre-cracked to its final length in accordance with ASTM E561-15a [23]. The load used for fatigue pre-cracking was limited to 25% of the fracture initiation load to prevent any plasticity that could affect the residual stress field. Finally, a small number of specimens of each type (indented and non-indented) had side-grooves cut as described in ASTM E399-12 [24] to promote straight crack front growth.

Four sets of specimens were tested: with side-grooves (with and without indentation), and without side-grooves (with and without indentation). The specimens were loaded to failure under displacement control. The Crack Mouth Opening Displacement (CMOD) was measured using an Instron 2670-132 extensometer (Instron Europe, High Wycombe, UK). Incremental unloading was used to enable the compliance method of crack length calibration [23]. Additional tests were interrupted at pre-determined CMODs and dye penetrant was used to measure the location of the crack front. The set of specimens that were not side-grooved developed a deeply-curved crack front during fracture (Fig. 3c), with shear lips forming at the surfaces. The side-grooved specimens maintained a straight crack front throughout the tests.

2.2. Neutron diffraction

Angle-dispersive neutron diffraction was performed on C(T) specimens using the SALSA instrument at the Institut Laue-Langevin [25]. This enabled measurement of elastic strains inside the specimens during fracture loading. Two specimens, one indented and one not indented, were loaded incrementally, pausing at regular increments of CMOD to perform mapping of the strain field surrounding the crack (see Fig. 3a). Another two specimens were loaded continuously while diffraction measurements were taken at a single location approximately

a.

b.
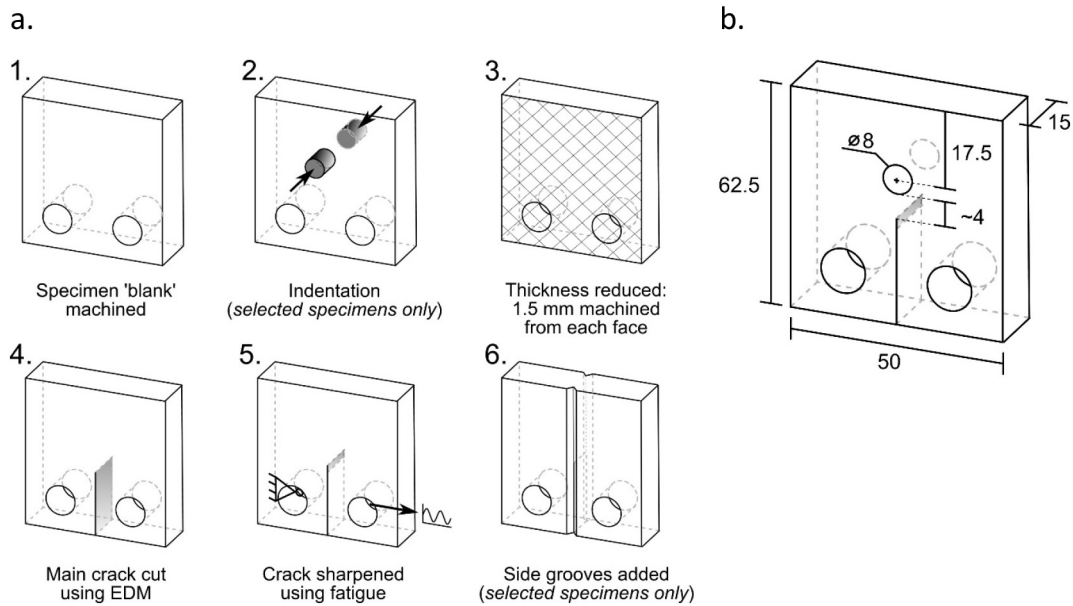
Fig. 1. a.) Preparation sequence for the C(T) specimens. Steps 2 and 6 were not performed on all specimens so four specimen sets were produced: indented with and without side-grooves, and non-indented with and without side-grooves. b.) Specimen dimensions and location of the indented region.

7.5 mm ahead of the initial crack tip (Fig. 3b). All neutron diffraction measurements were performed using specimens that were not side-grooved. Additionally, a uniaxial tension specimen of 7475-T7354 was loaded monotonically to failure while performing continuous neutron diffraction measurements. The equipment used for these measurements is shown in Fig. 2.

In the neutron diffraction measurements, the lattice spacing of the {311} plane family was measured using an incident neutron wavelength of 1.644 Å which resulted in scattering angles of $2\theta \approx 81.997°$. The gauge volume was defined as approximately $2 \times 2 \times 2$ mm using radial collimators and the unstrained lattice spacing was determined using a comb-type reference sample. Strain was measured in the loading direction only; the strain components in the crack propagation direction and the normal direction in C(T) specimens were not quantified. For the two incrementally-loaded C(T) specimens, strain field scans were taken at

0.5 mm increments of CMOD up to a maximum of 2.0 mm. The two continuously-loaded C(T) specimens were also loaded to a maximum CMOD of 2.0 mm. For both types of specimen, incremental unloading was used to enable the compliance method of crack length calibration [23].

2.3. Digital image correlation

Digital image correlation (DIC) was used to observe the deformation of the non-side-grooved C(T) specimens during the neutron diffraction experiments. The surface of each specimen was painted with a speckle pattern and a stereo pair of cameras recorded images of the surface throughout the experiment. These were related to an initial image, allowing the surface displacement field and hence the strain field to be calculated.
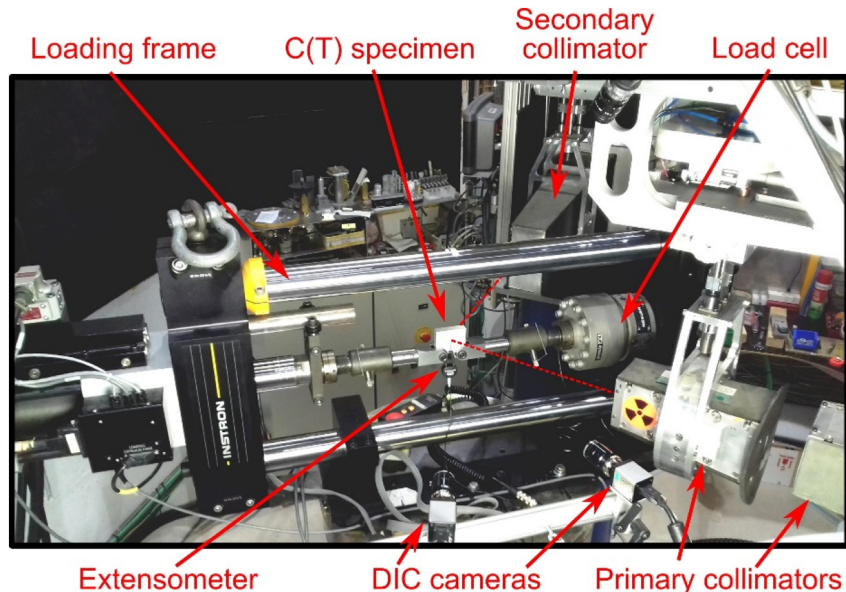
Fig. 2. Experimental setup for simultaneous neutron diffraction and digital image correlation measurements during fracture (SALSA beamline, Institut Laue-Langevin).

All DIC images were taken using a Dantec Dynamics Q-400 system (Dantec Dynamics GmbH, Skovlunde, DK) with two 5-megapixel (2448 × 2050), 8-bit grayscale cameras with Scheider Kreuznach Xenoplan-0902 lenses, 2.8/50 (relative aperture/focal length). The cameras were positioned as shown in Fig. 2, with a separation distance of approximately 300 mm and a standoff distance of approximately 500 mm, giving a scaling of 25 μm/px at the measured surface. The typical speckle size was approximately 6 pixels. Images were recorded continuously during loading at a rate of 1 Hz. The images were analysed using Istra 4D v4.4.2 software (Dantec Dynamics GmbH, Skovlunde, DK) using a facet size of 29 px and a facet spacing of 20 px.

2.4. Finite element analysis

Finite element analysis of the indentation and fracture loading of the C(T) specimens was performed using the Abaqus/Standard v6.12 finite element solver [26]. Mechanical constitutive properties of the specimen material were determined from the results of uniaxial tensile testing at ambient temperature (Fig. 4). The material was assumed to be homogeneous and isotropic, and it was modelled using incremental plasticity theory. It was also assumed to obey a non-linear isotropic hardening law with a von Mises yield locus. For the indented specimens, the complete sequence of indentation, surface removal, crack introduction and fracture loading was simulated. The indentation tool was modelled as a rigid body. Friction between the indenter and specimen was modelled using Coulomb's law with frictional coefficient of 0.5, which is an approximate value for unlubricated aluminium-steel contact [27]. The C(T) specimens without side-grooves were modelled using approximately 6000 4-noded tetrahedral linear elements and 32,000 8-noded linear brick elements. The side-grooved C(T) specimens were modelled using approximately 12,000 10-noded quadratic tetrahedral elements and 366,000 8-nonded linear brick elements. Sensitivity studies showed that the model results were insensitive to the frictional coefficient used and to further refinement of the finite element mesh.

The crack was modelled as existing in a single plane, neglecting out-of-plane crack deflection caused by the formation of shear lips close to the specimen's surface. Crack extension was modelled by incrementally releasing the symmetric boundary condition on the crack plane, accounting for the non-uniform crack growth across the specimen's thickness shown in Fig. 3c. No independent crack growth criterion was used. The crack length as a function of CMOD was already known from the physical fracture tests: both using the compliance calibration technique and from dye penetrant tests on broken-open specimens. Four types of specimens were used in the fracture tests (indented or not, side-grooved or not) and all four types were modelled. The different specimens exhibited different rates of crack extension as a function of CMOD, but the extension rate was very consistent for specimens of the same type (see Fig. 5).

FEA was used to find the distributions of plastic strain that resulted from indentation and fracture loading, and to determine estimates of the Rice J-integral for the crack tip [5]:

$$J = \int_{\Gamma} (W\delta_{1j} - \sigma_{ij}u_{i,1})n_j ds \qquad (4)$$

where Γ is a closed contour surrounding the crack tip, W is the strain energy density, δ_{ij} is the Kronecker delta, σ_{ij} is the stress tensor, u_i is the displacement vector and n_j is the normal vector to Γ. The J-integral characterises the crack tip stress field if the stress at all points within
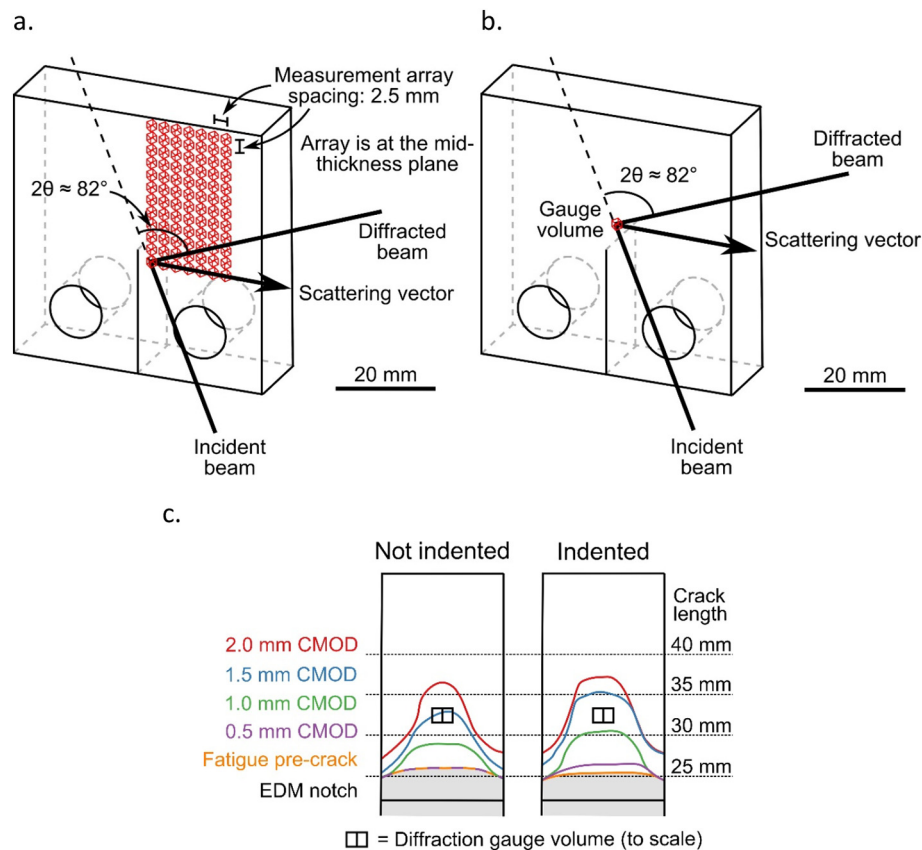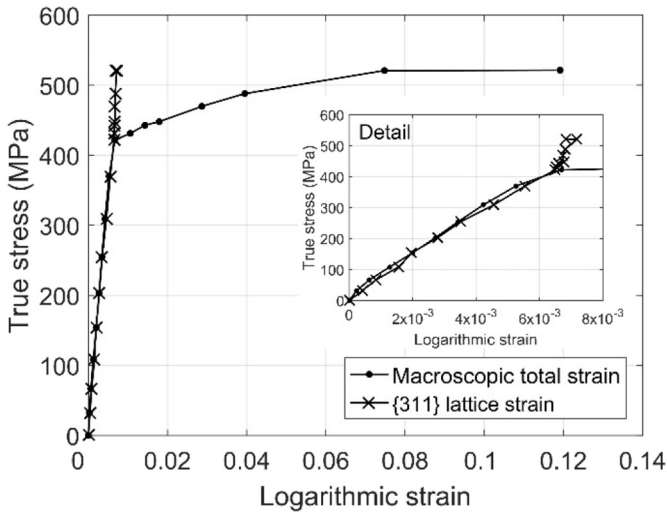

Fig. 3. Scattering geometry and gauge volume positioning used in the neutron diffraction measurements. a.) Mapping measurements, b.) continuous 'list mode' measurements ahead of the crack tip, c.) crack front propagation during continuous measurements.
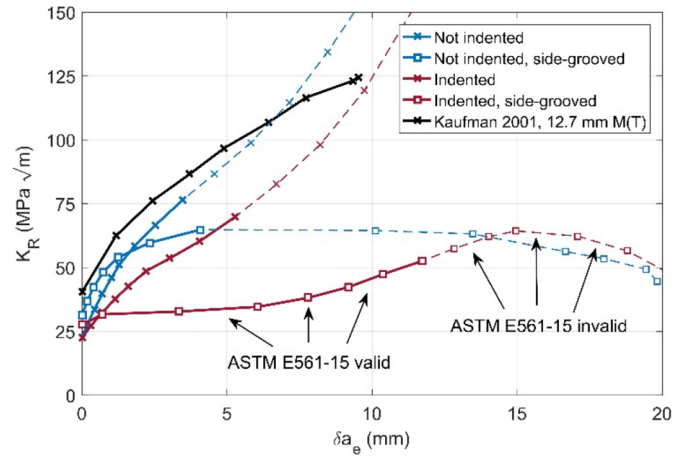
Fig. 4. Uniaxial tensile properties of aluminium alloy 7475-T7351, longitudinal to the rolling direction. Macroscopic strain from extensometer measurement, lattice strain from neutron diffraction.

Fig. 6. R-curves for aluminium alloy 7475-T7351 C(T) specimens with an overall thickness of 15 mm. Data in dashed lines do not satisfy ASTM E561–15 plastic zone size validity criterion [23]. Data from a previous study using 12.7 mm-thick M(T) specimens are shown for comparison [34].

the integration domain increases monotonically on a proportional loading path from zero [28]. Therefore the J-integral will not accurately characterise the crack tip stress field under the conditions assumed in this study: the specimen material is not modelled using constitutive relations which would ensure proportionality, and the specimens contain both moving cracks and initial stresses. However, despite these limitations J is used frequently for the approximate prediction of fracture initiation in real materials. In this study, the J-integral was calculated using the modified form suggested by Lei to account for an initial residual stress field [6,29]:

$$J_{mod} = \int_{\Gamma} \left(W\delta_{1j} - \sigma_{ij}u_{i,1}\right)n_j ds + \int_A \sigma_{ij}\varepsilon_{ij,1}^0 \, dA \qquad (5)$$

where A is the area enclosed by Γ and ε_{ij}^0 is the initial strain tensor. The first integral in Eq. (5) was re-formulated as an equivalent domain integral to enable extraction from the field results provided by FEA [30,31]. Throughout this study we extracted 'far-field' values of the J-integral from the FEA results [32], and used the recommendations given by Lei for calculating J_{mod} from the results of Abaqus/Standard FE analysis [33].

3. Results

3.1. Fracture tests

Fig. 5 shows the load-displacement behaviour of the C(T) specimens. In the experimental results, there is good repeatability within all specimen sets. Furthermore, there is a well-defined difference between the behaviour of indented and non-indented specimens. Non-indented specimens sustain a significantly higher maximum load. The results from FEA correspond well with the experimental data, albeit with minor differences. The curves from models of non-side-grooved specimens (Fig. 5a) are slightly low in comparison to the experimental dispersion; the most likely cause of this is that shear lip formation is not included in the models. The side-grooved specimens showed no shear lip formation and the modelling results for these specimens match the experimental data well, although deviate from it at the long crack extensions encountered beyond CMOD = 1.25 mm (Fig. 5b).

None of the data shown in Fig. 5 satisfy the specimen size requirements for calculation of the initiation fracture toughness K_{Ic} according to ASTM E399 [24]. However, fracture resistance curves for 7475-T7351 according to ASTM E561-15 [23] are shown in Fig. 6. Non-indented specimens exhibit a greater fracture resistance than indented ones across a range of effective crack extensions (δa_e). However,

a.

b.
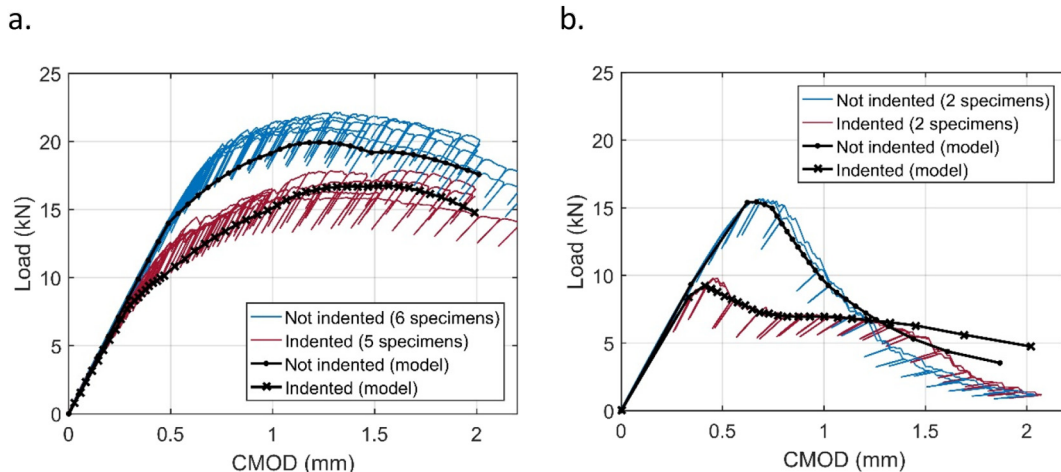
Fig. 5. Load vs. CMOD curves for aluminium alloy 7475-T7351 C(T) specimens with an overall thickness of 15 mm. a.) Not side-grooved, b.) side-grooved.
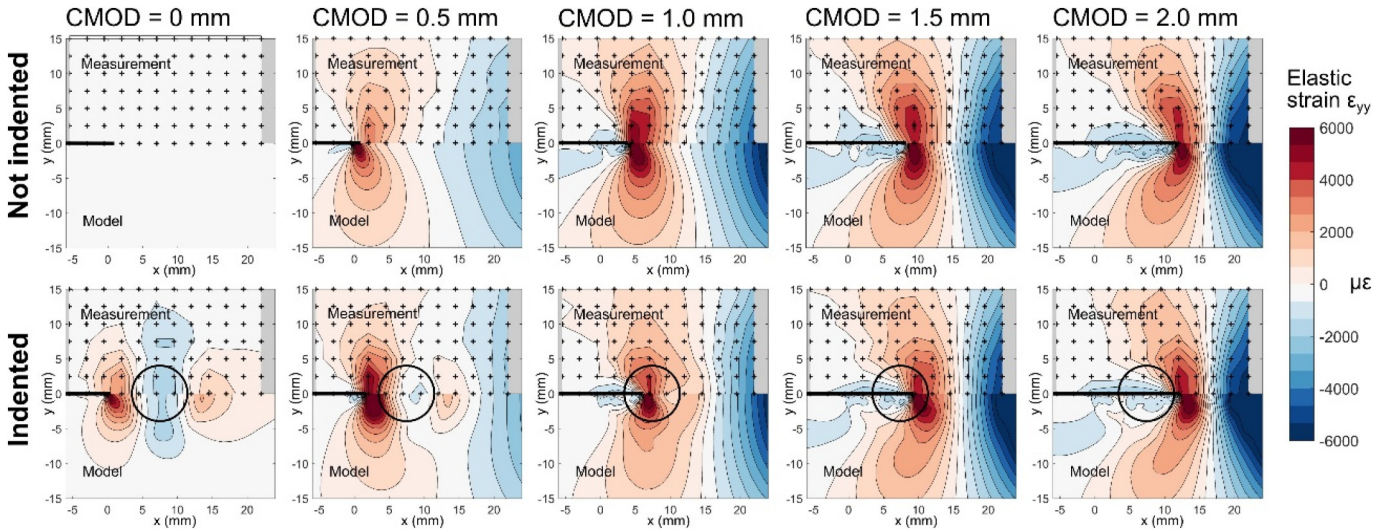
Fig. 7. Elastic strain at the mid-thickness plane in two aluminium 7475-T7351 C(T) specimens during fracture. The plots also show the extent of the crack at the mid-plane (black line), the indented region (black circle) and the neutron diffraction measurement locations (crosses). The experimental data are interpolated linearly between measurement locations. Only the crack-transverse strain component (ε_{yy}^{el}) is shown.

the R-curves for indented and non-indented side-grooved specimens do approach each other again at greater extensions. Side-grooving reduces the apparent fracture resistance by preventing constraint loss at the specimen surfaces, and so the R-curves for non-side-grooved specimens are higher than those for side grooved specimens at crack extensions >2 mm.

3.2. Neutron diffraction and DIC

Fig. 7 shows elastic strain on the mid-thickness plane of indented and non-indented specimens, comparing FEA predictions and neutron diffraction measurements. The error in the strain measurement due to diffraction peak-fitting uncertainty was evaluated to be approximately ±34 με [35]. The crack tip is initially at x = 0 mm and the crack extends to the right during the test. The residual elastic strain field measured in the indented specimen at CMOD = 0 mm shows good agreement with that predicted using FEA. The residual elastic strain field indicates the formation of a region of compressive residual stress under the indented area. The non-indented specimen is shown to be initially free from elastic strain, justifying the modelling assumption of an initially stress-free

sample. The progressive development of the elastic strain field during loading is also reflected accurately in the FEA results.

Elastic strain measured using neutron diffraction at a point initially 7.5 mm ahead of the initial crack tip is shown in Fig. 8a. The strain increases as the crack tip stress concentration approaches the diffraction gauge volume but then rapidly drops as the crack propagates through it. Similarly, the approaching crack tip stress field causes progressive broadening of the diffraction peak (Fig. 8b) as it increases the strain gradient inside the diffracting volume. The peak width reaches a maximum as the crack propagates through the gauge volume, after which the gradient in elastic strain is reduced and so the peak width decreases. Although the crack tip reaches the gauge volume earlier in the indented specimen than in the non-indented one, the maxima in elastic strain and FWHM are almost identical for the two specimens. This supports the concept of a material-invariant fracture process zone: regardless of conditions in the surrounding specimen, the stress state in direct proximity to the tip of the propagating crack is constant.

The total strain that develops on the surface of the specimens was measured using DIC and is shown in Fig. 9. As with the elastic strain data shown in Fig. 7, there is good agreement between the experimental

a.

b.
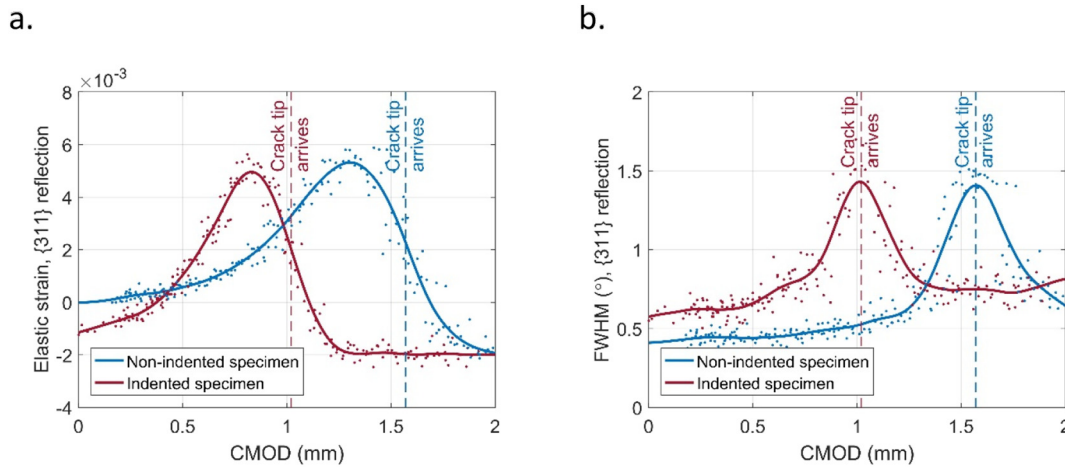
Fig. 8. Elastic strain and diffraction peak width in continuously-loaded C(T) specimens at the location shown in Fig. 3b–c (initially 7.5 mm ahead of the crack tip). Vertical dashed lines indicate when the crack tip has reached the centre of the diffraction gauge volume. a.) Elastic strain of the {311} plane family in the loading direction, b.) Full Width at Half Maximum (FWHM) of the {311} diffraction peak.
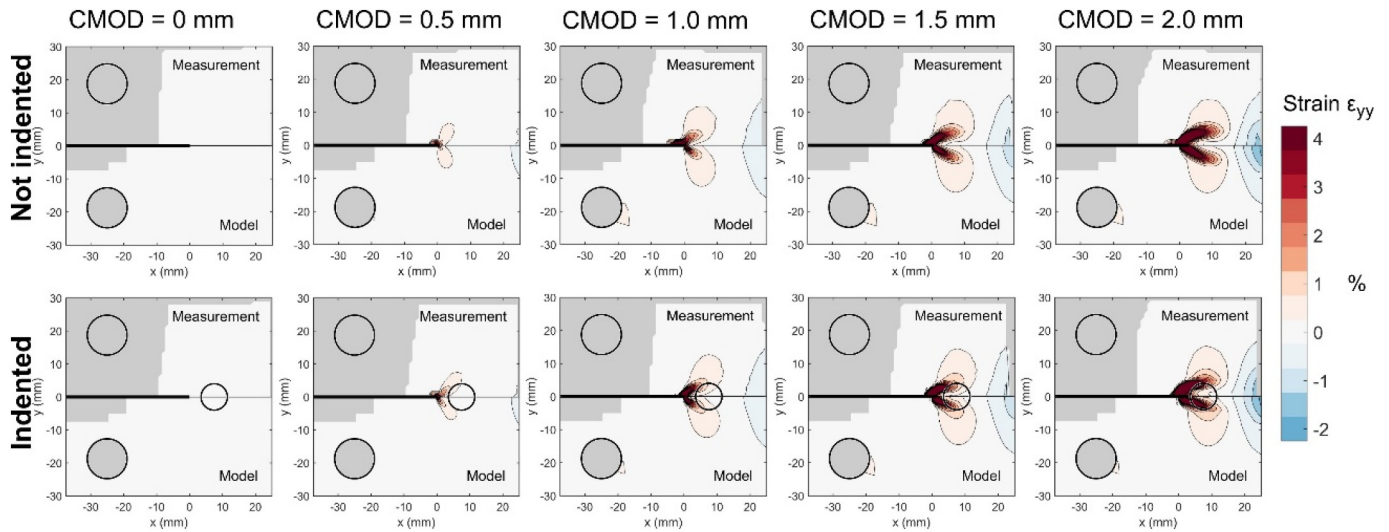
Fig. 9. Strain at the surface of two aluminium 7475-T7351 C(T) specimens during fracture. The plots also show the indented region (small circle) and the approximate extent of the crack at the surface (black line). Only the crack-transverse strain component (ε_{yy}) is shown. The reference configuration of the specimen for DIC was CMOD = 0 mm, so plastic strain accumulated during indentation and crack introduction is not included in the result.

data and the FEA prediction. The strain distributions that develop on the surface of indented and non-indented specimens are similar. At the surface, a lack of constraint in the out-of-plane direction promotes more extensive plasticity around the crack tip than occurs in the specimen interior. This loss of constraint against plasticity is also demonstrated by the tunnelling crack growth that occurs in non-side-grooved specimens (see Fig. 3c). Due to this lack of constraint, initial variations in residual stress and strain have little effect on the surface strain field. The good agreement between the FEA and experimental data presented in Figs. 7 and 9 demonstrates that the models provide a realistic representation of the physical specimens.

3.3. Plastic strain fields from FEA

Distributions of plastic strain inside the C(T) specimens were extracted from the results of finite element analysis. Fig. 10 shows the plastic strain field that develops in an indented and side-grooved specimen during the indentation and crack-cutting preparation steps (see also Fig. 1a). All plastic deformation is localised in and around the indented region. The initial tip of the crack prior to fracture loading extends almost into the volume of material that has been plastically deformed during indentation.
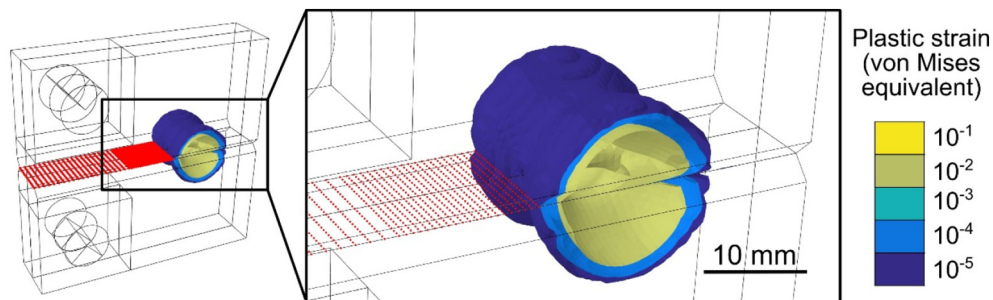
The plastic deformation that occurs during fracture of indented and non-indented side-grooved specimens is shown in Fig. 11. In the indented specimen, more plastic deformation occurs around the crack tip during the early stages of crack extension despite the lower applied

loads needed to achieve extension (see Figs. 5b and 6). At this point the crack tip loading is enhanced by the residual stress field. As the crack grows, the crack tip moves into the indented region which has experienced prior strain-hardening and contains a compressive residual stress transverse to the crack plane (see Fig. 7). Consequently, the crack propagates through the indented region with relatively little plastic deformation.

4. Discussion

Indentation of the fracture specimens creates a strong residual stress field and strain-hardens the compressed region. In side-grooved specimens prior to fracture testing, the maximum plastic strain on the fracture plane resulting from indentation is 3.0% which raises the material's yield stress locally by a maximum of 50 MPa. The residual stress field left behind directly after indentation has a large magnitude; FEA indicates that it reaches −470 MPa in the crack-normal direction. This results in a strong crack tip residual stress field after the crack is introduced (see Fig. 7).

Our observation that indentation ahead of the crack tip causes a lowering of the load-CMOD curve (see Fig. 5) is in agreement with previous studies by Mahmoudi et al. [36] Hurlston et al. [37] and Coules et al. [3] using similarly indented specimens. This effect occurs mainly because the residual stress field favours crack opening (Fig. 7): a positive Mode I stress intensity factor contributed by residual stress promotes fracture initiation and propagation during the first few millimetres of crack

Fig. 10. Initial plastic strain in a side-grooved C(T) specimen that occurs during indentation. The plane of the crack that is subsequently cut in the specimen (see Fig. 1a) is indicated by red dots. During loading, the crack grows into the pre-strained region.
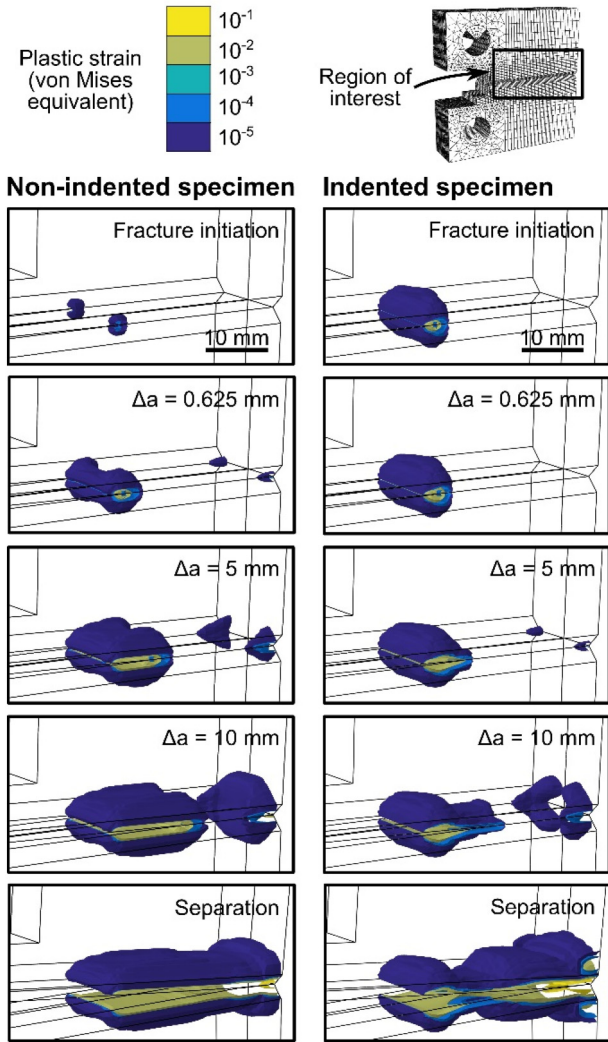
Fig. 11. Plastic wake development during crack propagation in side-grooved C(T) specimens of aluminium alloy 7475-T7351 subjected to monotonic loading. Only the incremental plastic deformation that occurs during fracture loading is shown; the prior strain caused by indentation and crack introduction is shown in Fig. 10.
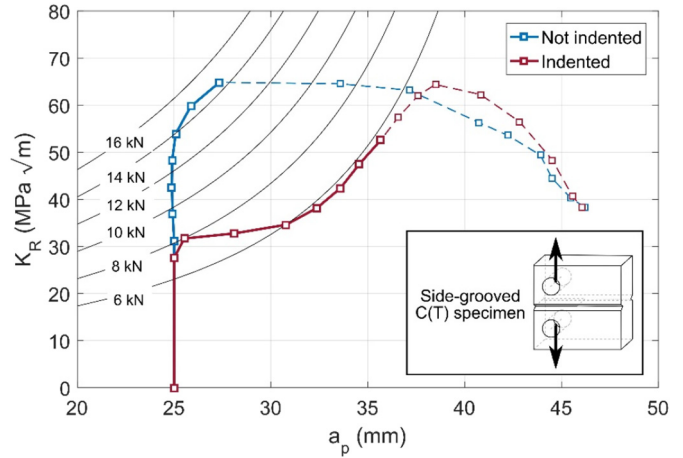

Fig. 13. Fracture stability in side-grooved C(T) specimens of 7475-T7351. Black lines show the Mode I stress intensity factor (as a function of crack length) that would be applied by loading the C(T) specimen with the indicated forces. Data in dashed lines do not satisfy the ASTM E561-15 plastic zone size validity criterion [23].

growth. Strain-hardening of material under the indented area may also reduce the specimen's fracture resistance. The region of material that is strain-hardened during indentation extends almost to the initial location of the crack tip (see Fig. 10). Therefore, in the indented specimens fracture initiates in material that has seen the same degree of strain-hardening as in the non-indented specimens. However, the crack propagates through material that has been significantly strain-hardened, i.e. the indented region.

Hill and VanDalen demonstrated that the R-curve for a similar aluminium alloy (7075-T6) can be corrected for residual stress in the test specimen using purely elastic assumptions [13]. This is supported by observations of initiation fracture toughness by Coules et al., who showed that limited plasticity occurs prior to fracture initiation in the same material subjected to residual stresses [3]. However, the specimens used in the present study had a higher initiation fracture toughness and contained a more severe residual stress field, so extensive plasticity occurred during crack propagation (Fig. 11).

Fig. 12 shows the result of adjusting the K_R curve measured from an indented (and side-grooved) fracture specimen for residual stress, using a correction based on linear elastic prediction of the effect of the
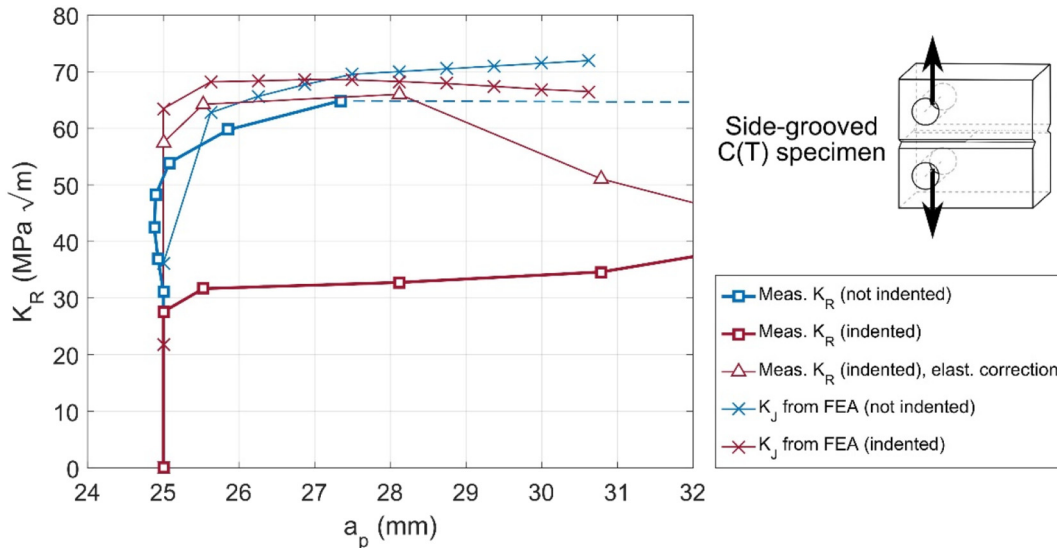

Fig. 12. Measured K_R and modelled crack tip K_J curves for side-grooved specimens as a function of the physical crack length a_p. For the indented specimen, an elastic superposition of the stress intensity factor contributed by residual stress (see Eq. (7)) with the measured "applied" K_R is also shown. Note the use of physical crack length (a_p) for the horizontal axis.

residual stress field on the crack. The distribution of residual stress on the prospective crack plane σ_{yy}^R, averaged through-thickness, was determined from the FE model of indentation after the model had been validated using the neutron diffraction measurements. The stress intensity applied by residual stress was calculated as a function of crack length a using the weight function method [38]:

$$K_I^R(a) = \int_0^a m(a, W, x)\sigma_{yy}^R(x)\, dx \tag{6}$$

where W is the C(T) specimen's characteristic length and m is its weight function [39]. The total stress intensity factor was then calculated by applying Eq. (1) at different crack lengths:

$$K_I(a) = K_I^A(a) + K_I^R(a) \tag{7}$$

where the applied stress intensity factor $K_I^A(a)$ is taken as $K_R(a)$ measured from an indented specimen. This approach of elastic correction gives good agreement with the K_R curve of a non-indented specimen for the first 3 mm of crack extension (see Fig. 12) but becomes less accurate as the crack advances and the plastic zone develops.

Extending Hill & VanDalen's approach, we calculated the elastic-plastic strain energy release rates for the same specimens by applying Eq. (5) to stress and strain field data from the elastic-plastic finite element models. It is noted that experimental measurements of crack length vs load and knowledge of the material's prior strain history were required as modelling inputs. The elastic-plastic equivalent stress intensity factor K_J was then calculated as a function of crack length using:

$$K_J(a) = \sqrt{J_{mod}(a)\, E'} \tag{8}$$

where E' is the materials' plane strain modulus and:

$$E' = \frac{E}{1 - \nu^2} \tag{9}$$

where E and ν are the material's elastic constants. Fig. 12 shows that the K_J vs crack extension curves for indented and non-indented specimens are similar despite their very different residual stress states (Fig. 7), load vs. displacement curves (Fig. 5b) and 'applied' K_R vs crack length curves (Fig. 13). This implies that a material-specific K_R curve that is independent of residual stress and prior plastic strain exists and can be derived even when fracture is not fully brittle. Deriving the K_R curve from a residually-stressed specimen in this way requires that the residual stress field is known and can be incorporated into an elastic-plastic finite element analysis. This result also implies that crack growth resistance curves measured in specimens without residual stress can be used to predict the propagation, arrest and stability of elastic-plastic fracture even in residually-stressed components, providing further support for the engineering practice of using J-based crack initiation and growth criteria for inelastic materials containing residual or thermal stresses [6,7,40].

Changes in the material's R-curve caused by residual stress affect the stability of a crack when it is subjected to external loading. A comparison of the fracture stability of two side-grooved specimens is shown in Fig. 13. Although the indented specimen eventually develops a crack growth resistance comparable to that of the non-indented specimen, it only does so after >10 mm of crack extension. This is due to the self-equilibrating residual stress field through which the crack grows (Fig. 7) which initially promotes crack-opening. After 10–15 mm of crack growth, the indented region has been separated by the crack and the strain misfit introduced there during indentation no longer acts to produce a residual stress. Consequently, the crack growth resistance at longer crack lengths is the same for the indented and non-indented specimens. In cracks that are subjected to a constant applied load, the stress

intensity factor resulting from that load increases with crack length (see Fig. 13). This effect counteracts the indented material's gently rising R-curve behaviour. As a result, the indented specimen is much more prone to unstable fracture: unstable crack growth will occur at a constant load of approximately 8 kN in an indented specimen, compared with approximately 15 kN for a non-indented one.

5. Conclusions

1. Residual stresses affect not only the fracture initiation behaviour of materials but also their resistance to subsequent crack growth, i.e. their R-curve. This can increase the susceptibility of cracks to unstable propagation.

2. In materials that exhibit non-brittle fracture, the effect of residual stress on the crack growth resistance for a given crack extension is not necessarily the same as the stress intensity factor calculated elastically from the initial residual stress. Plastic relaxation of residual stresses during crack extension modifies their effect on subsequent crack growth resistance.

3. The modified J-integral formulation (J_{mod}) due to Lei performs well as a predictor of elastic-plastic crack advance under residually-stressed conditions. More generally, our experimental results support the use of J_{mod} for the analysis of cracks propagating under these conditions, even though it may not accurately characterise the crack tip stress field.

4. An elastic-plastic correction for determining a material's R-curve using fracture test data from a residually-stressed specimen has been demonstrated. This method requires the use of inelastic finite element analysis in addition to characterisation of the specimen's initial residual stress field and strain hardening state.

5. Elastic strains measured at the tips of growing cracks in residually-stressed and non-residually stressed material were observed to be the same, even when the surrounding stress field differed. This supports the concept of a near-tip stress field that can be characterised using a very limited number of parameters.

Data availability statement

The data required to reproduce these findings are available to download from: https://doi.org/10.5523/bris.2hzzpi1of2n3j2mc3lqs5k2ywe.

References

[1] P.J. Withers, Residual stress and its role in failure, Rep. Prog. Phys. 70 (12) (2007) 2211–2264.
[2] P.J. Budden, J.K. Sharples, Treatment of secondary stresses, in: R.A. Ainsworth, K.-H. Schwalbe (Eds.), Comprehensive Structural Integrity, 1st ed., vol. 7, Elsevier-Pergamon 2003, pp. 245–288.
[3] H.E. Coules, D.J. Smith, P.J. Orrock, K.A. Venkata, T. Pirling, A combined experimental and modelling approach to elastic-plastic crack driving force calculation in the presence of residual stresses, Exp. Mech. 56 (8) (2016) 1313–1325.
[4] P.M. James, P. Hutchinson, C.J. Madew, A.H. Sherry, Predictions of elastic-plastic crack driving force and redistribution under combined primary and secondary stresses - part 2: experimental application, Int. J. Press. Vessel. Pip. 101 (2013) 91–100.
[5] J.R. Rice, A path independent integral and the approximate analysis of strain concentration by notches and cracks, J. Appl. Mech. 35 (1968) 379–386.
[6] Y. Lei, J-integral evaluation for cases involving non-proportional stressing, Eng. Fract. Mech. 72 (4) (2005) 577–596.
[7] R6: Assessment of the Integrity of Structures Containing Defects, Revision 4, Amendment 11. , EDF Energy, Gloucester, 2015.
[8] BS 7910:2013 - Guide to Methods for Assessing the Acceptability of Flaws in Metallic Structures. , BSi, 2013.

[9] R.A. Ainsworth, Failure assessment diagram methods, in: R.A. Ainsworth, K.-H. Schwalbe (Eds.), Comprehensive Structural Integrity, 1st ed., vol. 7, Elsevier-Pergamon 2003, pp. 89–132.

[10] T.L. Anderson, Fracture Mechanics: Fundamentals and Applications, CRC Press, 2005.

[11] J.E. Strawley, W.F. Brown, Fracture toughness testing methods, Fracture Toughness Testing and Its Applications, ASTM Special Technical Publication No. 381, ASTM 1964, pp. 133–196.

[12] X.-K. Zhu, J.A. Joyce, Review of fracture toughness (G, K, J, CTOD, CTOA) testing and standardization, Eng. Fract. Mech. 85 (2012) 1–46.

[13] M.R. Hill, J.E. VanDalen, Evaluation of residual stress corrections to fracture toughness values, J. ASTM Int. 5 (8) (2008) 101713.

[14] T.H. Becker, M. Mostafavi, R.B. Tait, T.J. Marrow, An approach to calculate the J-integral by digital image correlation displacement field measurement, Fatigue Fract. Eng. Mater. Struct. 35 (10) (2012) 971–984.

[15] A.J. Moore, J.R. Tyrer, Phase-stepped ESPI and Moire interferometry for measuring stress-intensity factor and J integral, Exp. Mech. 35 (4) (1995) 306–314.

[16] M.N. James, M.N. Pacey, L.-W. Wei, E.A. Patterson, Characterisation of plasticity-induced closure - crack flank contact force versus plastic enclave, Eng. Fract. Mech. 70 (2003) 2473–2487.

[17] R. Picon, F. Paris, J. Canas, J. Marin, A complete field method for photoelastic determination of KI and KII in general mixed mode fracture, Eng. Fract. Mech. 51 (3) (1995) 505–516.

[18] H.E. Coules, G.C.M. Horne, M.J. Peel, S.J. Oliver, D.G.A.V. Gelderen, T. Connolley, Direct observation of elastic and plastic strain fields during ductile tearing of a ferritic steel, Proceedings of the ASME 2016 Pressure Vessels & Piping Conference, 2016 (no. 63345).

[19] A. Steuwer, M. Rahman, A. Shterenlikht, M.E. Fitzpatrick, L. Edwards, P.J. Withers, The evolution of crack-tip stresses during a fatigue overload event, Acta Mater. 58 (11) (2010) 4039–4052.

[20] P.J. Withers, Fracture mechanics by three-dimensional crack-tip synchrotron X-ray microscopy, Phil. Trans. R. Soc. A 373 (2015) 20130157.

[21] P. Lopez-Crespo, M. Mostafavi, A. Steuwer, J.F. Kelleher, T. Buslaps, P.J. Withers, Characterisation of overloads in fatigue by 2D strain mapping at the surface and in the bulk, Fatigue Fract. Eng. Mater. Struct. 39 (8) (2016) 1040–1048.

[22] ASTM E1823-10a, Standard terminology relating to fatigue and fracture testing, ASTM International, 2010.

[23] ASTM E561-15a, Standard Test Method for KR Curve Determination, ASTM International, 2015.

[24] ASTM E399-12e3, Standard test method for linear-elastic plane-strain fracture toughness K_{Ic} of metallic materials, ASTM International, 2012.

[25] T. Pirling, G. Bruno, P.J. Withers, SALSA - a new instrument for strain imaging in engineering materials and components, Mater. Sci. Eng. A 437 (1) (2006) 139–144.

[26] Abaqus/Standard v6.12, Dassault Systemes Simulia Corp., Providence, RI, USA, 2012.

[27] E.A. Avallone, T. Baumeister, Marks' Standard Handbook for Mechanical Engineers, 10th ed. McGraw-Hill, 1996.

[28] M. Kuna, Finite Elements in Fracture Mechanics: Theory - Numerics - Applications, Springer, 2013.

[29] R.A. Ainsworth, D.G. Hooton, R6 and R5 procedures: the way forward, Int. J. Press. Vessel. Pip. 85 (3) (2008) 175–182.

[30] C.F. Shih, B. Moran, T. Nakamura, Energy release rate along a three-dimensional crack front in a thermally stressed body, Int. J. Fract. 30 (2) (1986) 79–102.

[31] Abaqus Theory Guide v6.12, Dassault Systèmes, 2012.

[32] W. Brocks, I. Scheider, Reliable J-values: numerical aspects of the path-dependence of the J-integral in incremental plasticity, Materialprufung 45 (2003) 264–275.

[33] Y. Lei, Validation of contour integral functions (J and C(t)) in ABAQUS v6.11–v6.14 for combined mechanical and residual stresses, Structural Integrity Procedia 2 (2016) 2566–2574.

[34] J.G. Kaufmann, Fracture Resistance of Aluminum Alloys, ASM International, 2001.

[35] ISO, 21432:2005 - Non-destructive Testing: Standard Test Method for Determining Residual Stresses by Neutron Diffraction, No. ISO 21432:2005, ISO, 2005.

[36] A.H. Mahmoudi, C.E. Truman, D.J. Smith, Using local out-of-plane compression (LOPC) to study the effects of residual stress on apparent fracture toughness, Eng. Fract. Mech. 75 (13) (2008) 1516–1534.

[37] R. Hurlston, J.K. Sharples, A.H. Sherry, Understanding and accounting for the effects of residual stresses on cleavage fracture toughness measurements in the transition temperature regime, Int. J. Press. Vessel. Pip. 128 (2015) 69–83.

[38] H. Tada, P.C. Paris, G.R. Irwin, The Stress Analysis of Cracks Handbook, 3rd ed. Professional Engineering Publishing, 2000.

[39] X.R. Wu, A.J. Carlsson, Weight Functions and Stress Intensity Factor Solutions, Pergamon Press, 1991.

[40] W.K. Wilson, I.-W. Yu, The use of the J-integral in thermal stress crack problems, Int. J. Fract. 15 (4) (1979) 377–387.